# Comparison of Electrochemical Degradation for Spray Dried and Pulse Gas Dried $LiNi_{0.5}Mn_{1.5}O_4$

**Matthias Seidel,[1] Muthuraman Kugaraj,[1] Kristian Nikolowski,[1,z] Mareike Wolter,[1] Isabel Kinski,[2] Thomas Jähnert,[3] and Alexander Michaelis[1,2,4]**

[1] *Fraunhofer Institute for Ceramic Technologies and Systems IKTS, Dresden, Saxony, Germany*
[2] *Fraunhofer Institute for Ceramic Technologies and Systems IKTS, Hermsdorf, Thuringia, Germany*
[3] *Glatt Engineering, Weimar, Thuringia, Germany*
[4] *Technische Universität Dresden, Dresden, Saxony, Germany*

To commercialize next-generation cathode materials a lot of different synthesis methods need to be researched and evaluated regarding the attainable electrochemical properties of the materials on one hand, and the scalability of the process on the other. For the high voltage $LiNi_{0.5}Mn_{1.5}O_4$ cathode material especially the degradation of the material during cycling needs to be investigated for different scales and techniques. $LiNi_{0.5}Mn_{1.5}O_4$ (LNMO) was synthesized using two different methods in different scales: lab-scaled spray drying and pilot-scaled gas pulse drying. The materials were analysed by XRD, FESEM, particle size distribution and BET to achieve an extensive overview of the particles. The electrochemical properties were examined by galvanostatic charging and discharging at different C-rates as well as EIS at different SOCs using $LiNi_{0.5}Mn_{1.5}O_4$/Li coins cells. To improve the electrochemical properties additional grinding and temperature treatments were used. Their influence on the electrochemical properties was investigated by analysing the capacity slippage as well as the electrolyte-, surface film- and the charge transfer resistance. These results will show that the same electrochemical properties can be achieved for the $LiNi_{0.5}Mn_{1.5}O_4$ cathode material when changing and upscaling the synthesis methods.

 [DOI: 10.1149/2.0621913jes]

Manuscript submitted May 15, 2019; revised manuscript received August 13, 2019. Published August 22, 2019.

Lithium-ion batteries have been a focus of research since their introduction to the consumer market in the early 1990s. Especially with the change in communication technologies and the need for small portable devices they have become more essential, because of their high energy and power density. Therefore, lithium ion technology became a prime source of energy for electronic and portable devices. Today, lithium ion technology plays also a significant role in the automotive sector. For the application as a car battery, even higher energy and power density are necessary to become competitive with fuel-powered cars, especially regarding the drivable distance per battery charge. This improvement can mostly be achieved by enhancing the battery system and the components used. One of the most significant components, which has to be improved to reach this goal, is the active material of the cathode.[1]

The technological advancement in the areas of mobile energy storage demands a low-cost, environment-friendly, thermally stable lithium-ion battery with high energy density. To achieve higher energy density an improved specific capacity and/or high potential is necessary. Concerning its higher potential, the spinel $LiNi_{0.5}Mn_{1.5}O_4$ (LNMO) is a promising candidate for cathode materials. LNMO has a potential plateau at 4.7 V vs $Li/Li^+$ and a theoretical specific capacity of 147 mAh/g.[2] Furthermore, using LNMO the costs of the raw materials can significantly be reduced, since it contains no cobalt. Another advantage is that LNMO is less toxic than cobalt based cathode materials. Moreover, the spinel structure exhibits a high structural stability because of isotropic expansion and contraction during the intercalation process.[3] Depending on the distribution of the nickel and manganese atoms, LNMO can form two space groups with ordered and disordered crystal structure. In the ordered structure (space group of primitive cubic structure $P4_332$), Ni and Mn atoms occupy the 4a and 12d sites respectively, while in the disordered structure (space group of face-centered cubic structure $Fd\bar{3}m$), both types of the atoms are randomly distributed in the octahedral 16d sites.[4] The disordered crystal structure can provide better electrochemical properties and stability than the ordered crystal structure.[5–7] For that reason, the aim was to synthesize and investigate the disordered crystal structure in this study.

The electrochemical performance of this cathode material is significantly influenced by two parameters: the amount of $Mn^{3+}$ ions and the presence of the $Li_yNi_{1-y}O$ rock salt phase.[2,8] The formation of disordered LNMO is usually accompanied by a rock salt phase that lowers the obtainable capacity of the cathode material.[9] Another challenge is the ability to control the degree of $Mn^{3+}$ions as it is redox-active and improves the conductivity of LNMO. But if the amount of $Mn^{3+}$ is too high and two $Mn^{3+}$ ions can interact one will become $Mn^{2+}$ and other will become $Mn^{4+}$. This is known as a disproportionation reaction.[10] Furthermore, $Mn^{2+}$ is soluble in the electrolyte and $Mn^{4+}$ is stable and electrochemically inactive on further lithium extraction.[11] It results in poor performance of LNMO and capacity fading. Nevertheless, the conductivity of the disordered LNMO is enhanced with small amounts of $Mn^{3+}$ resulting in improved rate capability.[12]

To obtain an optimized cathode material, a synthesis method needs to be developed which is able to produce LNMO in an industrial scale, and at the same time, to manufacture a material with a low amount of impurity phases like $Li_yNi_{1-y}O$ rock salt phase, the appropriate $Mn^{3+}$ content as well as well-formed particles with a defined particle size.[13] In this study LNMO materials were synthesized by two different synthesis methods: spray drying and APPtec Advanced Pulse Powder Technology (Glatt GmbH). This study investigated whether the different morphologies and $Mn^{3+}$ content of the synthesized LNMO materials lead to differences in the electrochemical performance. Aside from the two different synthesis routes it was also studied whether additional calcination and grinding steps have an influence on the electrochemical performance.[7,14]

The materials developed using the above-mentioned methods were thoroughly characterized and tested to understand the influence of different synthesis routes on the electrochemical performance. Dahn et al. illustrated that the undesired reactions occurring inside the cell because of the high voltage are a major challenge for the commercialization of high voltage cathode materials.[15] The undesired reactions lead to electrolyte decomposition, low coulombic efficiency and increased internal resistance over the cycle, significantly affecting the lifetime of the battery.[16–18] By preparing test cells from produced samples the cumulative endpoint slippage capacity and electrochemical impedance spectroscopy were investigated to measure and distinguish the undesired reaction occurring in the cell.[19–21] The electrochemical impedance spectroscopy (EIS) technique was used to study the influence of the crystal lattice on the electrochemical properties.[22,23]

[z] E-mail: kristian.nikolowski@ikts.fraunhofer.de

**Table I. LNMO samples synthesized under different conditions (AT*: pilot scale "pulse gas" method (APPtec), ST*: lab scale "spray drying", *L*: educts used as solution, *S*: educts used as suspension, *0: no additional temperature treatment, *5: additional 5 h temperature treatment, *5g: additional 5 h temperature treatment with preceding grinding)**

| Additional calcination | APPtec solution | APPtec suspension | Spray drying |
|---|---|---|---|
| Without additional calcination | AT_L_0 | AT_S_0 | ST_L_0 |
| 5 h 800°C treatment | AT_L_5 | AT_S_5 | ST_L_5 |
| 60 min grinding; 5 h 800°C treatment | AT_L_5g | AT_S_5g | ST_L_5g |

## Experimental

***Synthesis.—***LNMO was synthesized using two different synthesis methods, which are suitable to produce the cathode material in different scales:

The pulse gas method is a synthesis route which was developed by Glatt GmbH. In this method, a solution or suspension with different precursor compositions and characteristics is sprayed into a pulse gas environment with an adjustable droplet size distribution.[24] The pulsing gas flow creates special thermodynamic reaction conditions providing the produced powders with superior properties. As a result of this defined thermal treatment, desired chemical and mineralogical reactions take place and particles are formed. Duration of the thermal treatment is less than 10 seconds. Table I gives an overview of the synthesized material.[24]

The materials prepared by the pulse gas method (APPtec) are abbreviated with AT. Additionally, they are marked with an 'S' if a suspension-based precursor was sprayed, and marked with an 'L' for a solution-based precursor.

For the spray drying method, a homogeneous precursor was produced by dissolving stoichiometric amounts of $CH_3COOLi \cdot 2H_2O$ (99%, Sigma-Aldrich), $Ni(CH_3COO)_2 \cdot 4H_2O$ (99%, Sigma-Aldrich) and $Mn(CH_3COO)_2 \cdot 4H_2O$ (99% Sigma-Aldrich) in ethanol. The solution was sprayed via a Büchi Mini Spray Dryer B-290 to produce the precursor. The precursor was heated with 1°C/min to 200°C followed by 5°C/min to 800°C and held at a temperature of 800°C for 5 h under air in a muffle furnace. After the holding time, the materials were cooled down overnight in the oven. The materials which were synthesized by spray drying are named ST in Table I.

***Grinding and calcination treatment.—***Additional temperature treatment, i.e. a second calcination step, was applied to some of the samples (marked with "5"). It was carried out in a muffle oven. The samples were heated with 1°C/min to 200°C followed by 5°C/min to 800°C and hold for a duration of 5 h. After the holding time, the materials were cooled down in the oven overnight. Furthermore, some samples (marked with a G) were ground before the second calcination. Grinding was carried out for 60 min in a planetary ball milling machine (Fa. FRITSCH GmbH) with EtOH as grinding medium.

***Characterization.—***SEM images from the synthesized LNMO powders were taken using a Crossbeam NVISION 40 from Carl Zeiss SMT with an Everhart Thornley detector. XRD data were measured using a Bruker D8 diffractometer with $CuK_\alpha$ (0.154056 nm) radiation. The samples were placed on a flat sample holder and measured in Bragg-Brentano geometry. The phase analysis of the patterns was carried out using the program "DIFFRAC.EVA". For electrochemical measurements, electrodes were prepared by casting a slurry of 80% active material ($LiNi_{0.5}Mn_{1.5}O_4$), 10% binder (PVDF, Solef) and 10% carbon (Super P, Timcal) on an Al foil (Hydro) and drying it for 20 h at a temperature of 60°C. The electrodes were calendared to reach a porosity of approximately 30%. Afterwards, coin cells with a two electrode setup were prepared as half cells against metallic lithium. Whatmann glass fibre discs were used as separator and LP40 (1M $LiPF_6$ in EC:DEC 1:1 w/w, BASF) was used as an electrolyte. The assembled coin cells $LiNi_{0.5}Mn_{1.5}O_4$/Li were galvanostatically cycled between 3.5 and 5.0 V. All electrochemical measurements were conducted at 30°C using a BASYTEC cell testing system. For each synthesized LNMO material, 5 coin cells were prepared to get a reliable mean value. The coin cells which were used for the galvanostatic measurement were used for EIS measurement as well. EIS was done using the Gamry framework version 6.25 integrated with Basytec CTS at 30°C. The EIS measurements were performed with 10 mV perturbation amplitude in the range from 100 kHz to 1 Hz in automatic sweep mode from high to low frequencies. The impedance was measured at a SOC of 90%, 60%, 30% and 10%. Before the impedance was applied at each SOC, the potential was stabilized for 2 h. The generated impedance was further fitted using the function ZfitGUI (varagin) from Matlab software using the equivalent circuit which is mentioned in Figure 12.

## Result and Discussion

***Material characterization.—****XRD.*—To determine whether the spinel phase was formed during the different synthesis methods XRD measurements were carried out. The disordering of LNMO is related to the formation of oxygen vacancies that occurs when the sample is annealed at elevated temperatures of more than 700°C.[25] Figure 1 shows the diffraction pattern of all samples. The reflections of the crystal planes are highlighted and are characteristic for the LNMO crystal phases.[12,26] It can be seen that the samples show different phase purities depending on their synthesis method. The samples without additional calcination show either a low crystallization, which can be detected by broad reflections with low intensity for the "pulse gas" samples (AT_L_0 and AT_S_0), or several additional reflections for the "spray drying" samples (ST_L_0), which cannot be attributed to the spinel phase reflections. The spinel phase reflections are indicated by their indices. Impurities are marked by arrows in Figure 1 and can be assigned to the rock-salt-phase $Li_xNi_{1-x}O$. The weak reflections at 37.5°, 43.7°

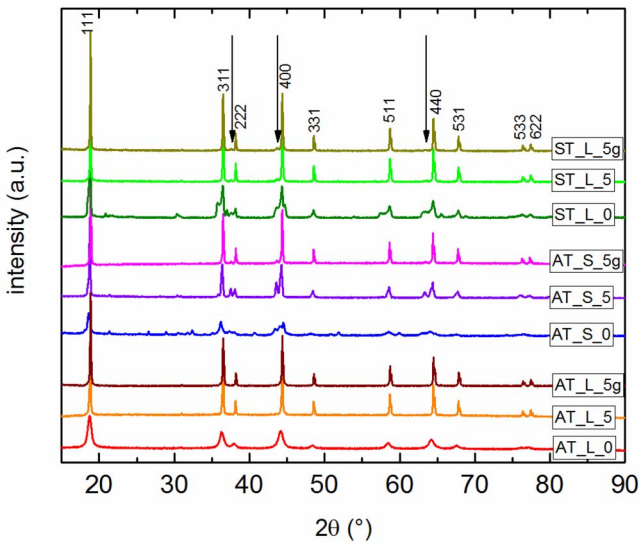


**Figure 1.** XRD patterns of $LiNi_{0.5}Mn_{1.5}O_4$ samples in the 2θ range from 10° to 90°. Impurity phase $Li_xNi_{1-x}O$ highlighted by black arrows.

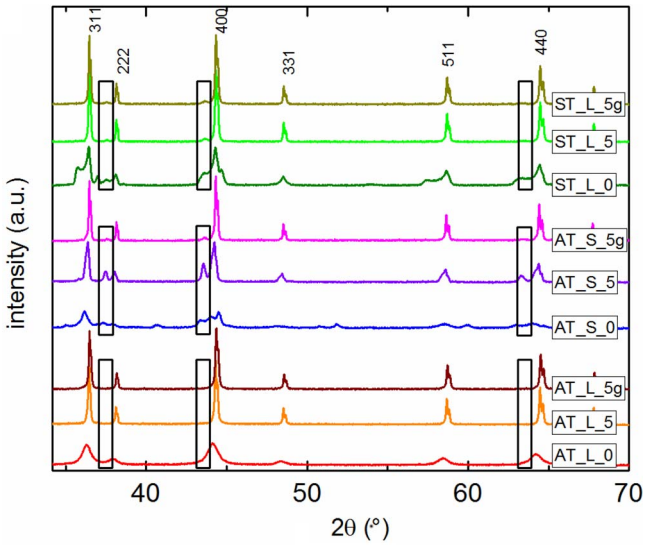


**Figure 2.** XRD patterns of $LiNi_{0.5}Mn_{1.5}O_4$ materials in the 2θ range from 35° to 70°. Impurity phase $Li_xNi_{1-x}O$ highlighted by black boxes.

and 63.7° indicate the rock salt phase $Li_xNi_{1-x}O$, which is often detected along with the LNMO disordered crystal structure.[27] In Figure 2 the reflections of the phases are highlighted with black boxes. It can be seen that the reflection's intensities are different and thus, the amount of impurity phase is different for the samples. Additional calcination contributed to improving the crystallization which can for example be seen comparing the untreated (AT_L_0) with the treated (AT_L_5) "pulse gas" solution sample. Additional calcination and grinding also helped to reduce the amount of impurity phase considering the treated (AT_S_5, ST_L_5) and untreated samples (AT_S_0, ST_L_0). The quantity change of the rock-salt phase is based on the visual intensity change (Figure 2, black boxes). Grinding has a significant influence on some materials. Especially as seen in Figure 2, the "pulse gas" suspension samples (AT_S) show a significant change of the intensity of the reflections of the impurity phase. By applying this treatment the amount of impurity was reduced. A change could not be detected for the other samples. The impurity phase probably was reduced, because the oxygen contact to the surface of the material was improved through the intermittent grinding step. Nevertheless, the atmosphere (air), calcination duration and temperature influence the reintegration of the rock salt phase into the spinel structure. Therefore, additional calcination, grinding and enhancement of the oxygen contact to the sample surface further improved the crystallization. While the influence of grinding is minor on the solution based samples (ST_L and AT_L), which already show low amounts of rock-salt phase, grinding shows further improvement for samples with a high amount of rock-salt phase (AT_S_5). Overall, a low amount of impurity phase was detected for the samples with additional grinding and heating step (*_5g).

*FESEM.*—FESEM images were made to investigate the difference regarding the particle morphology, size and texture. The images are shown in Figure 3. It can be seen that additional calcination has a great influence on the particles. Before additional calcination, especially for the "pulse gas" samples (AT_L, AT_S) no crystal planes can be seen. For the "spray drying" samples (ST_L) some crystal planes are visible, but no clear crystal forms like octahedrons can be detected. Through additional calcination, crystals were formed as can be seen in Figure 3. Additionally, the materials show different particle shapes. The "pulse gas" samples show smaller particles. For the treated "pulse gas" solution samples (AT_L_5), especially, the size per particle is around 0.1 μm. For the treated "pulse gas" suspension samples (AT_S_5) the size is around 1 μm. Even bigger particles can be seen for the treated "spray drying" samples (ST_L_5) reaching a size of more than 1 μm. Clear crystal planes can be seen after additional calcination. The materials mostly have octahedron shapes. The samples with additional grinding show no significant change. Therefore, additional grinding has only a small influence on the particle size level. It rather has more impact on aggregation and agglomeration of the materials. Overall, it can be concluded that additional calcination is needed to form and to grow crystals. The "pulse gas" suspension (AT_S) and "spray drying" solution (ST_L) samples show a clear octahedron shape which is the preferred shape for spinel. This means that the homogeneously distributed metal ions during additional calcination support the formation of these defined crystal planes.

*Particle size distribution/BET.*—Figure 4 shows the particle size distribution of all materials and its change during the subsequent grinding and temperature treatments. It can be seen that there is no change in the particle size distribution for the "pulse gas" solution samples (AT_L). The "pulse gas" suspension samples (AT_S), however, show different particle sizes after additional calcination. The "pulse gas" samples with no treatment (AT_S_0) and with treatment (AT_S_5) reveal two particle sizes. One peak is around 1 μm and the other one is around 30 μm. After grinding the size distribution of the "pulse gas" suspension sample (AT_S_5g) is further reduced and a particle size around 2.5 μm is predominant. From the results, it can be seen that the "pulse gas" solution samples show smaller particle size distributions than the "pulse gas" suspension samples. A change in particle size distribution can also be seen for the "spray drying" (ST_L) samples: from a wide distribution with two peaks for the untreated samples (ST_L_0) to a much smaller distribution with one peak after grinding and additional calcination (ST_L_5g). The treatment helps to break up aggregates leading to a more homogeneous distribution.

The d90 and the specific surface which were measured by BET are shown in Figure 5. The results are arranged in three different columns for the different methods. For the "pulse gas" solution samples (AT_L) there is no difference in the particle size distribution (d90), but a change in the specific surface can be detected. By additional calcination, the surface was largely reduced from 20 $m^2/g$ to around 4 $m^2/g$. Grinding did not influence on the "pulse gas" solution sample (AT_L_5g). With 7 $m^2/g$ the specific area for untreated "pulse gas" suspension samples is lower compared to the untreated "pulse gas" solution samples (AT_L_0). The specific area is also reduced to 1 $m^2/g$ by additional calcination (AT_S_5) and to 2 $m^2/g$ by grinding (AT_S_5g). The "spray drying" (ST_L) samples show no change in the specific surface with values around 1–3 $m^2/g$, but a reduction of the particle size distribution. The particle size distribution d90 is reduced from 38 to 6 μm. Additional grinding influences the particle size distribution of "pulse gas" solution samples (AT_L_5g), but the specific surface did not change. Overall, additional calcination and grinding lead to a reduction in particle size and of the specific surface area. The measurements of the particle size distribution (laser diffraction) and specific surface area (BET) do not provide information on the individual surfaces of the primary particles, the results rather represent the aggregates and agglomeration of the particles. Both samples which were produced by the "pulse gas" method (AT_S and AT_L) show a high surface area before any additional treatment. No visible particle growth occurred because the structure is heavily influenced by the fine distribution during spraying. After additional calcination crystals form and bigger particle lead to the surface area reduction. For the "spray drying" (ST_L) samples no significant changes in specific surface area can be seen, because particles have already been formed. The change in the particle size distribution is very different. It needs to be pointed out that the materials were handled differently for the analytic methods. For the particle size distribution, the powders were dispersed in a solution. Agglomerates were broken up and therefore a difference to the BET measurements can be seen, where the agglomerates are still existing. For the "pulse gas" solution samples (AT_L) the particle size distribution does not change, but by the additional treatment agglomerates are removed. The "pulse gas" samples with additional calcination (AT_S_5) show no differences in the particle size. Only

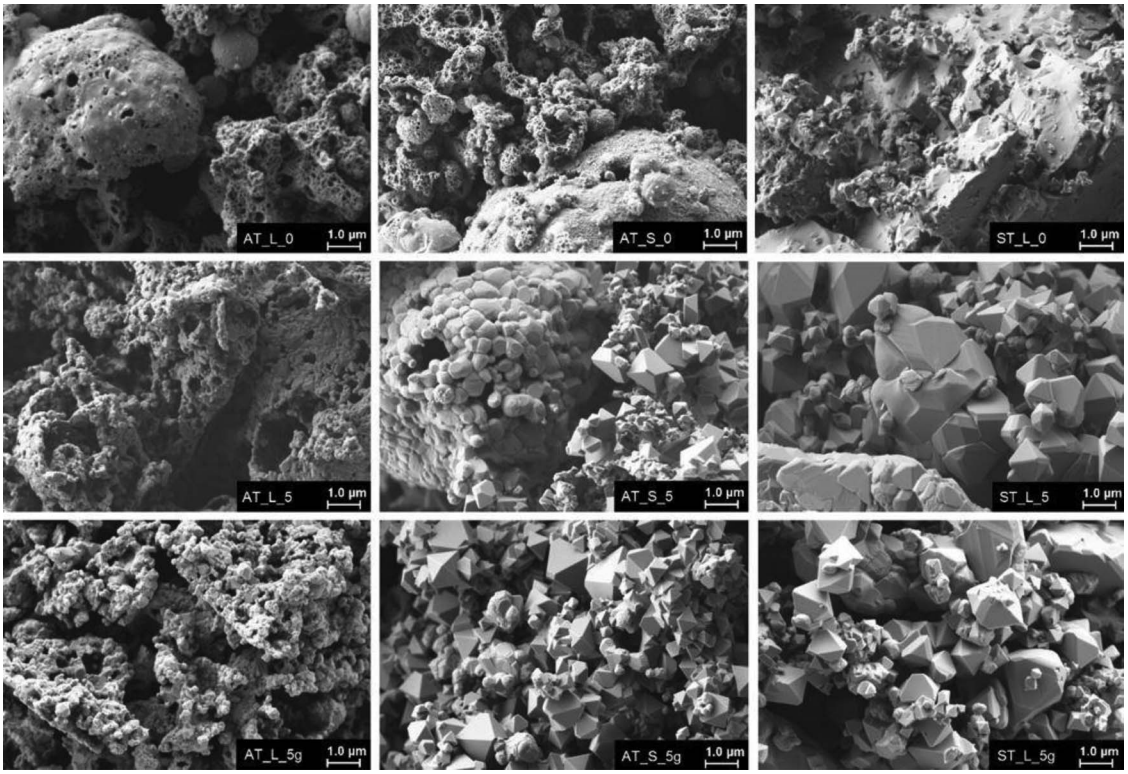


**Figure 3.** FESEM images of the different $LiNi_{0.5}Mn_{1.5}O_4$ samples.

after grinding the size of the particles could be reduced and aggregates could be broken up. Regarding the surface, the properties are similar to the "pulse gas" solution samples (AT_L) leading to a similar conclusion regarding the formation of crystals. For the "spray drying" samples (ST_L) additional calcination led to smaller particles. This can be described by the fact that big aggregates form smaller particles. The FESEM pictures also show this change in Figure 3.

***Electrochemical characterization.—****Galvanostatic cycling properties.*—The electrochemical performance for four different C-rates and the cycling stability over 20 cycles were characterized using a galvanostatic method. The rate capability for all samples is shown in Figure 6. The rate capability was calculated with respect to the 2nd discharge capacity, because for several samples the capacity showed a significant difference between first and second discharge. The materials show a significant difference in the specific capacity at the measured C-rates. Additional calcination led to significantly improved values as shown in Figure 6. Grinding has also a positive influence on the specific capacity. It can be seen that the increase is different for the samples. The untreated "pulse gas" suspension sample (AT_S_0), especially, has a very low capacity with 41 mAh/g, whereas the "pulse gas" (AT_L_0) and "spray drying" (ST_L_0) solution samples show a capacity of 100 mAh/g and 81 mAh/g respectively. The specific capacity can be tripled after calcination for the "pulse gas" suspension sample (AT_S_5), and increases by

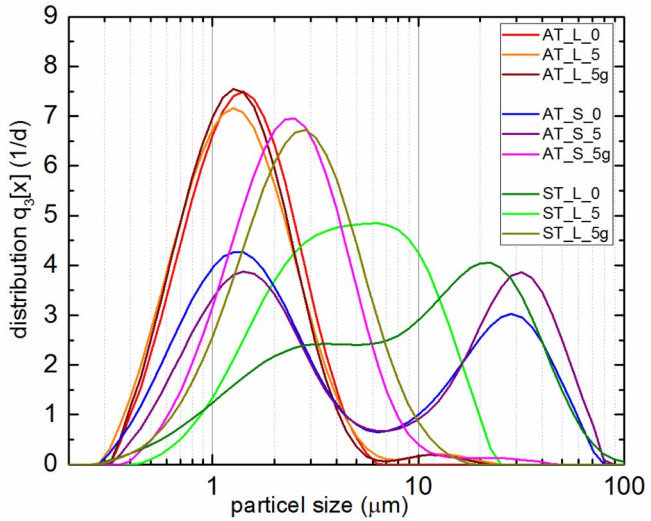


**Figure 4.** Particle size distribution of different $LiNi_{0.5}Mn_{1.5}O_4$ samples.

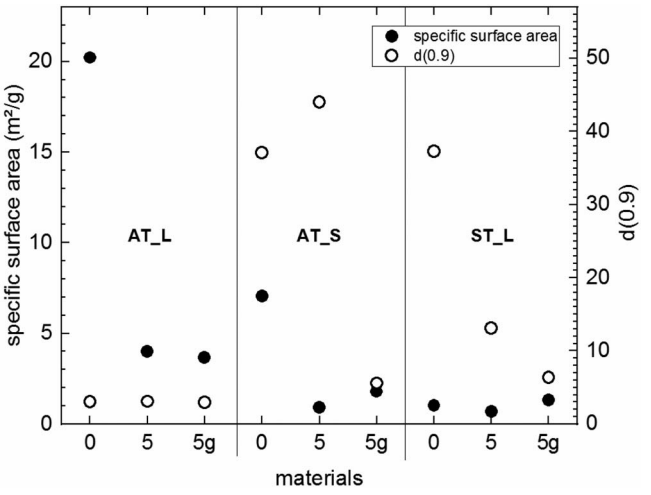


**Figure 5.** Overview of the specific surface and the particle size distribution (d90) of $LiNi_{0.5}Mn_{1.5}O_4$ samples.

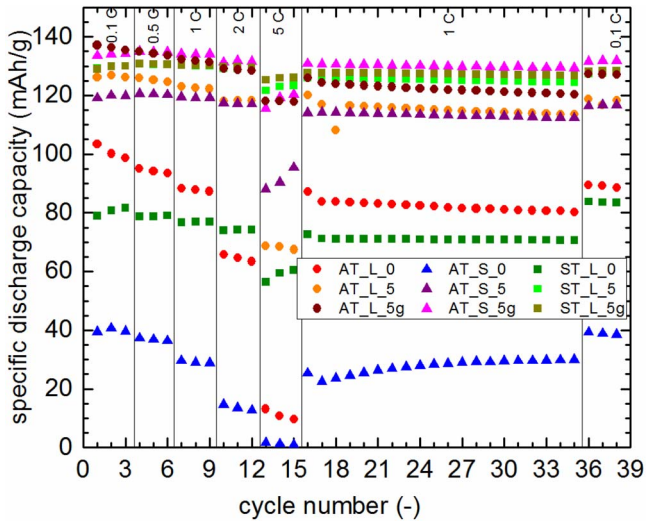


**Figure 6.** Rate capability and aging tests results for $LiNi_{0.5}Mn_{1.5}O_4$ samples.

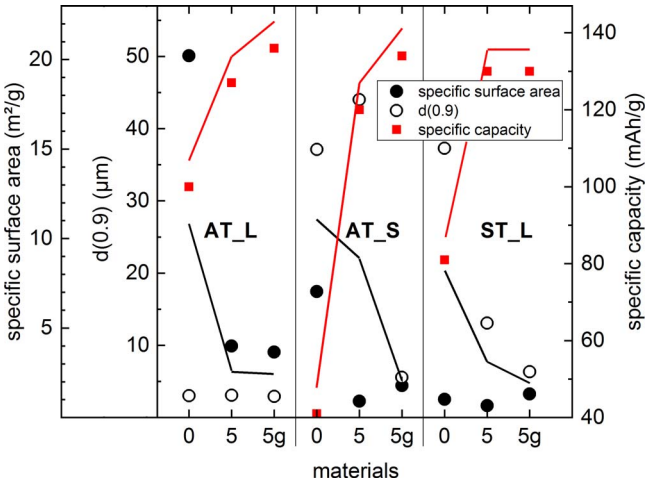


**Figure 7.** Overview of the specific surface and the particle size distribution (d90) of $LiNi_{0.5}Mn_{1.5}O_4$ samples correlated to the specific discharge capacity at 0.1 C. The dashed lines are only guide for the eyes. To illustrate the correlation the combined change of the surface and the particle size were indicated with a black line (line of guidance). The change to the capacity is indicated by a red line (line of guidance).

27% and 60% for the "pulse gas" solution (AT_L_5) and "spray drying" (ST_L_5) samples, respectively. Additional grinding does not influence the specific capacity for the "spray drying" sample (ST_L_5g), but increases the specific capacity for the "pulse gas" samples (AT_L_5g, AT_S_5g) as shown in Table II. The reduction in capacity over different C-rates was calculated from Figure 6 and summarized in Table II. In general, the materials which have undergone additional calcination as well as grinding show less capacity reduction with increasing C-rate. The specific capacity generally drops with increasing C-rate. But, depending on the materials properties and synthesis method, the amount by which the capacities drops is very different. The specific capacity correlates to the particle size distribution. The electrolyte can reach a higher amount of the active material surface for the samples with smaller particles and therefore reduces diffusion pathways.

In Figure 7 the specific surface and the particle size distribution is correlated to the specific capacity measured. Both material properties influence the electrochemical properties. A high surface area and/or low particle size results in a lower specific capacity, which can be an indication for more active sides were parasitic reactions can occur and/or lithium which is not fully integrated into the structure and therefore not electrochemically active. This can especially be proved by the samples without any additional treatment (*_0). The highest capacity of more than 130 mAh/g was reached for samples with additional treatment (*_5g). For those samples, small particle size and specific surface were achieved.

With an increase of the C-rate from 0.1 C to 1 C the "pulse gas" suspension samples (AT_S) and "spray drying" samples (ST_L) with additional treatment show no significant capacity reduction. This also applies for an increase to 2 C, where only the "pulse gas" suspension sample (AT_S) shows a small drop of 1–2%. At a C-rate of 5 C the capacity decreases significantly for all samples except for the "spray drying" samples (ST_L_5, ST_L_5g) showing the lowest reduction with only 5% and 3% respectively. Some values regarding the electrochemical properties are shown in Table II. Only the ground "spray drying" sample (ST_L_5g) has lost just 1% of its initial capacity after 38 cycles in total, which is comparatively less as compared to the other materials. In contrast, a huge reduction in capacity was measured for the materials which were not subjected to additional calcination (AT_L_0, AT_S_0 and ST_L_0). The materials having bigger particles exhibit less specific discharge capacity reduction than materials with smaller particles. The difference in size can not only be measured like indicated by the PSD (Figure 7) but also be seen in Figure 3 with clear different sized particles.

This leads to the interpretation that materials with higher surface area and/or smaller particle size show stronger interaction with the electrolyte during charge/discharge cycling, subsequently resulting in higher capacity fading. The materials which possess a uniform particle size distribution (Figure 4) show less reduction in capacity than materials with a non-uniform distribution. The more uniform particle size distribution correlates with the reduction of very large particles, which are not able to fully intercalate and deintercalate lithium, because of limited lithium transport into bigger particles. In addition to litera-

**Table II. Electrochemical values measured by galvanostatic cycling at different C-rates. Capacity increase due to additional treatment relative to untreated sample, C-rate change, aging over 20 cycles at 1 C charge and discharge and capacity retention after the performance and aging test. Manganese(III) amount determined from the relative capacity between 3.5 and 4.5 V.**

| | Specific capacity at 0.1C [mAh/g] | Capacity increase due to additional treatment [%] | 0.1 C to 1 C [%] | 0.1 C to 2 C [%] | 0.1 C to 5 C [%] | Aging after 20 cycles [%] | 0.1 C capacity retention [%] | $Mn^{3+}$ amount [%] |
|---|---|---|---|---|---|---|---|---|
| AT_L_0 | 100 | - | 12 | 35 | 89 | 5 | 11 | 50 |
| AT_L_5 | 127 | 27 | 3 | 7 | 46 | 3 | 8 | 9 |
| AT_L_5g | 136 | 7 | 3 | 5 | 13 | 3 | 7 | 8 |
| AT_S_0 | 41 | - | 29 | 66 | 98 | −30 | 5 | 86 |
| AT_S_5 | 120 | 192 | 1 | 2 | 24 | 1 | 2 | 47 |
| AT_S_5g | 134 | 12 | 0 | 1 | 10 | 1 | 1 | 23 |
| ST_L_0 | 81 | - | 5 | 9 | 26 | 1 | −4 | 34 |
| ST_L_5 | 130 | 60 | 0 | 0 | 5 | 1 | 1 | 12 |
| ST_L_5g | 130 | 0 | 0 | 0 | 3 | 1 | 1 | 8 |

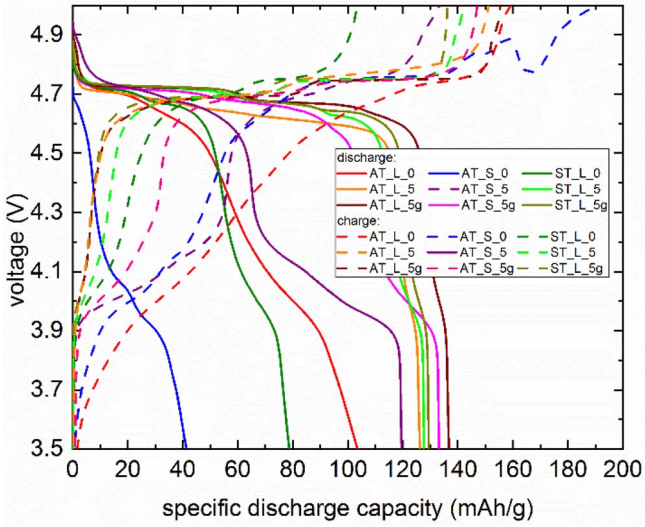


**Figure 8.** 1st charge/discharge curves of $LiNi_{0.5}Mn_{1.5}O_4$ samples at 0.1 C (3.5–5 V, 30°C).

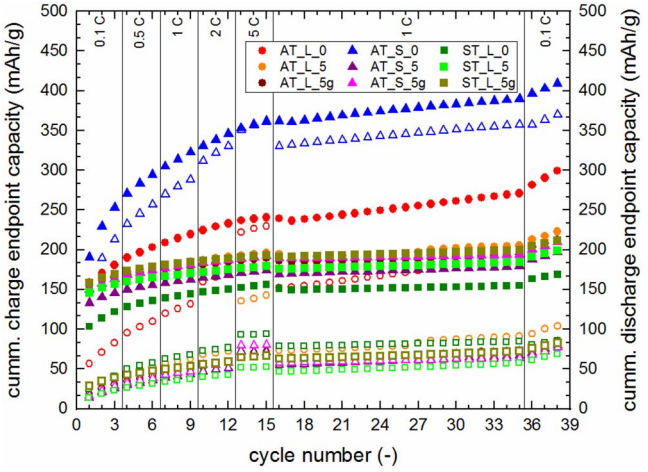


**Figure 9.** Cumulative end point capacities of $LiNi_{0.5}Mn_{1.5}O_4$ samples determined by galvanostatic measurements. (charge: full symbol, discharge: empty symbol; 3.5–5 V, 30°C).

ture results, the octahedron crystal shape has enhanced electrochemical properties as compared with other crystal shapes (Figure 3).[28] Apart from material properties, the reduction in specific capacity is influenced by the different synthesis routes. From Figure 6 it can be seen that the reduction in capacity is much lower for the untreated "spray drying" sample (ST_L) as compared to the "pulse gas" samples (AT_*). As mentioned in the experimental section, the extended calcination, with the first calcination lasting for 5 h and not seconds like for the pulse gas method, the time of the "spray drying" method allows sufficient time to form the crystal planes during preliminary calcination (ST_L). For the "pulse gas" method, the spraying time is much shorter (less than 10s), and thus, does not allow the crystal planes to form during preliminary calcination, leading to the higher reduction in capacity.

The amount of $Mn^{3+}$ can be estimated from the plateau in the voltage range of 3.5 V - 4.5 V on the charge/discharge voltage curve as shown in Figure 8. It was assumed that at 4.5 V all $Mn^{3+}$ was oxidized to $Mn^{4+}$. The $Mn^{3+}$ percentage of all materials was calculated on the basis of the second discharge because of formation reactions during the first cycle. The first charge shows a significantly higher capacity than the first discharge. This is especially pronounced for the "pulse gas" sample AT_S_0 which additionally shows a voltage drop at above 4.7 V (Figure 8). This effect is only observed during the first cycle and may be related to formation reactions seen in Figure 1 and Figure 2 (AT_S_0). The values for the manganese(III) content are summarized in Table II. The "pulse gas" samples (AT_L_0, AT_S_0) which show a high amount of $Mn^{3+}$ percentage of 50% and 86%, respectively, covering more than half of the voltage curve in the voltage region of 3.5 V–4.5 V, whereas for all other materials the voltage plateau at 4.7 V is much more dominant. The materials with a high $Mn^{3+}$ amount (AT_L_0, AT_S_0 and ST_L_0) consequently have poor electrochemical performance. Additional calcination and grinding reduce the $Mn^{3+}$ amount. It is expected that grinding increases the oxygen interaction during additional calcination. This may lead to the enhanced particle growth and to the reduction of the $Mn^{3+}$ amount. Additional calcination led to a significant reduction of the $Mn^{3+}$ amount by 39% for the "pulse gas" suspension material (AT_S_5), by 8.5% for the "pulse gas" solution sample (AT_L_5) and by 11.7% for the "spray drying" (ST_L_5) sample. Additional grinding has less influence on the $Mn^{3+}$ reduction for the solution samples (AT_L_5g, ST_L_5g), whereas the $Mn^{3+}$ amount could be reduced by another 24% for the suspension samples (AT_S_5g) as shown in Table II. In general, "pulse gas" suspension samples (AT_S) possess higher $Mn^{3+}$ amounts than the other materials. This must be due to the reason that the surface contact between the individual precursor particles to oxygen is comparatively smaller during the calcination process as compared to solution-based materials. Also the distribution of the educts in the suspension is not even, which results in long diffusion ways and in the end an inhomogeneous phase formation. This leads to a higher $Mn^{3+}$ amount for suspension based materials.

*Cumulative endpoint slippage.*—The above-mentioned correlations between the material and the electrochemical properties encourage to further investigate the phenomena of electrolyte decomposition at the surface of the high voltage cathode material $LiNi_{0.5}Mn_{1.5}O_4$ samples synthesized (4.7 V vs $Li/Li^+$). Electrolyte decomposition is caused by undesired side reactions. This can lead to the formation of a cathode electrolyte interphase (CEI) which can hinder the lithium ion transport from electrolyte to active material. These undesired reactions differ according to the specific material and its morphology (crystal presence, particle size, and crystal structure).[28,29]

The cumulative charge and discharge end point capacities of all materials, determined by galvanostatic measurements, are presented in Figure 9. During the cycling of the cells, the charge and discharge capacities do not exactly match due to parasitic currents, so that the curves shift sequentially from one cycle to the next. Generally, the more the curves slip right the more parasitic reactions have occurred.[19] This shift between the cycles is referred to as capacity slippage. The cumulative capacity represents the specific capacity of the specific cycle as well as the slippage of every previous cycle. The more the cumulative capacity differs from the measured capacity (charge) or zero (discharge) at the given cycle the more side reactions occurred until the given cycle. It is therefore a degree for the occurred side reactions. The value of the cumulative endpoint capacities increases up to the 13–15th cycle, which correspond to 5 C discharge. Afterwards, the cumulative endpoint capacity increases again from the 16th to the 38th cycle, corresponding to the 1 C/1 C cycling. Even though these material have been discharged with different C-rates over the entire program, it is still reliable to distinguish the amount of parasitic reaction occurring in the cell considering the magnitude of endpoint capacity (Y-axis) at the end of the cycles. The difference between the charge and discharge end point capacity provides the specific capacity of the cell at a particular cycle. The capacity slippage (slope of the curve) is much higher at initial cycles (1–3) than in the mid or at the end of the cycles. This is most likely due to the formation of a solid electrolyte interface which profoundly occurs in the initial cycles leading to a reduced growth rate in the consecutive cycles. The magnitude of the parasitic reaction is also strongly dependent on the time of exposure of the electrode to the electrolyte. The values discussed were taken after the measured 38 cycles and reflect the sum of the

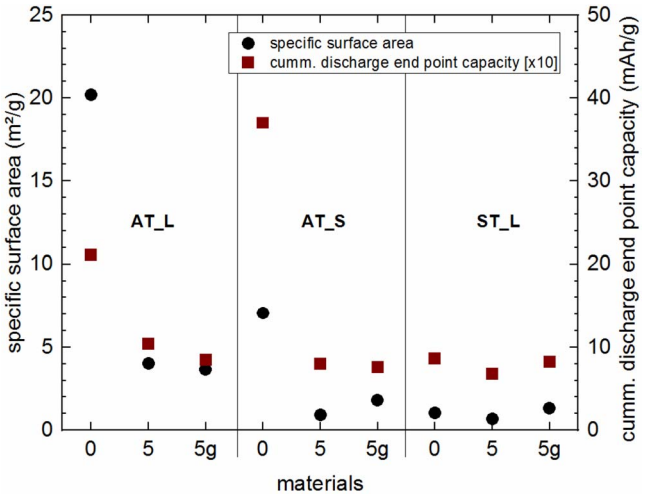


**Figure 10.** Correlation between specific surface area and cumulative discharge of $LiNi_{0.5}Mn_{1.5}O_4$ samples.

side reactions which occurred during the measurement program. From Figure 9 it can be seen that the untreated "pulse gas" suspension sample (AT_S_0) has a very high cumulative discharge endpoint capacity of 370 mAh/g, whereas the solution samples (AT_L_0, ST_L_0) have a cumulative discharge endpoint capacity of 211 mAh/g and 86 mAh/g, respectively. By additional calcination the cumulative discharge endpoint capacity was significantly reduced to 80 mAh/g for the "pulse gas" suspension sample (AT_S_5), to 104 mAh/g for the "pulse gas" solution sample (AT_L_5) and to 68 mAh/g for the "spray drying" sample (ST_L_5). Additional grinding has no significant influence on the cumulative discharge endpoint capacity for the "pulse gas" samples (AT_S_5g, AT_L_5g), but the cumulative discharge endpoint capacity slightly increased for the "spray drying" sample (ST_L_5g) as shown in Figure 9. The same interpretation may be applied for the cumulative charge endpoint capacity. The magnitude of the parasitic reaction is strongly influenced by the specific material properties. The values of the additionally treated samples can be related to values reported in the literature. The capacity slippage for LNMO was reported to be slightly over 50 mAh/g after 28 cycles at 30°C and with a C-rate of 0.1 C.[16] Most of the presented samples show a value between 53 and 86 mAh/g and therefore exhibits similar degradation. Nevertheless is has to be pointed out that the experiments were carried out using different C-rates.

From Figure 10 it can be seen that the cumulative discharge endpoint capacity linearly responded according to the specific surface area of the material. This must be due to the electrolyte and electrode interface which seems to be high when the material has more surface area. This higher interface leads to more electrolyte decomposition and subsequently to a higher capacity slippage. In Figure 10, the cumulative discharge endpoint capacities values were plotted in the magnitude of 10 [x10]. Apart from the specific surface area, the presence of crystals has also a strong influence on the capacity slippage. The "spray drying" samples (ST_L) show reduced capacity slippage as compared to the "pulse gas" samples (AT_S, AT_L). This might be related to the presence of crystal plains after preliminary calcination. For "pulse gas" samples, by contrast, there is no crystal plains present after preliminary calcination. From those correlations, it can be assumed that it is recommended to have a particle size not less than 1 μm in order to obtain optimum electrochemical performance and reduced electrolyte decomposition. It can be concluded that the electrolyte decomposition is heavily influenced by the specific surface area of the material (Figure 10). To reduce capacity fading and the kinetic hindrance, a uniform particle size distribution as well as appropriate particle sizes are necessary.

The synthesis parameters and the sample properties discussed are summarized in Table III.

*EIS.*—Electrochemical impedance spectroscopy measurements provide information about the lithium ion transport in the electrodes as well as on the interface properties. The ability of lithium ion transport is controlled by the kinetic properties as well as the electrode reaction. These factors are strongly influenced by the material morphology. The sequence of transport includes the transport processes for lithium ions, electrons, and the charge transfer process. Due to the differences in the time constants between these processes, EIS is a suitable technique to investigate these reactions and to separate these phenomena.[30] Therefore, using EIS and equivalent circuit analysis the parameters related to lithium ions insertion/extraction process in intercalation materials such as surface film resistance, charge transfer resistance and electrolyte resistance can be studied. The varying frequency was applied on the galvanostatically cycled coin cells at the different states of charge. From Figure 11 it can be seen that for the materials with different morphology, the width of the semi-circles varies. All the materials Nyquist plots at a SOC of 90% are marginally different from the other state of charges. At a SOC of 90%, the untreated "spray drying" material (ST_L_0) has a very low impedance value as compared to the "pulse gas" samples (AT*). This must be due to the presence of crystal planes after preliminary calcination, whereas the untreated "pulse gas" samples (AT_L_0, AT_S_0) do not exhibits crystal presence after preliminary calcination (Figure 3). As shown in Figure 11, the surface film and charge transfer impedance values are significantly reduced after additional calcination and grinding. According to the interpretation of material and electrochemical properties, the impedance values are strongly dependent on the development of the crystal phase. The materials which possess a homogeneous and fully developed crystal phase exhibits reduced charge transfer impedance values as compared to the other materials.

To further analyze the generated impedance information and to understand the correlation between material morphology and kinetic characteristics, an equivalent circuit analysis was carried out. The information of electrolyte resistance, surface film resistance, and the

**Table III. synthesis parameters and properties for the analyzed samples (*60 min PKM grinding, **one step represents a calcination at 800°C).**

| | methode | grinding* | calcination steps** | Specific capacity at 0.1C [mAh/g] | $Mn^{3+}$ amount [%] | specific surface area [$m^2$/g] | cumm. discharge end point capacity [x10] | d(0.9) [μm] |
|---|---|---|---|---|---|---|---|---|
| AT_L_0 | APPtec solution | no | 1 | 100 | 50 | 20.2 | 21 | 3 |
| AT_L_5 | APPtec solution | no | 2 | 127 | 9 | 4.0 | 10 | 3 |
| AT_L_5g | APPtec solution | yes | 2 | 136 | 8 | 3.7 | 8 | 3 |
| AT_S_0 | APPtec suspension | no | 1 | 41 | 86 | 7.9 | 37 | 37 |
| AT_S_5 | APPtec suspension | no | 2 | 120 | 47 | 0.9 | 8 | 44 |
| AT_S_5g | APPtec suspension | yes | 2 | 134 | 23 | 1.8 | 8 | 6 |
| ST_L_0 | Spray drying | no | 1 | 81 | 34 | 1.1 | 9 | 37 |
| ST_L_5 | Spray drying | no | 2 | 130 | 12 | 0.7 | 7 | 13 |
| ST_L_5g | Spray drying | yes | 2 | 130 | 8 | 1.4 | 8 | 6 |

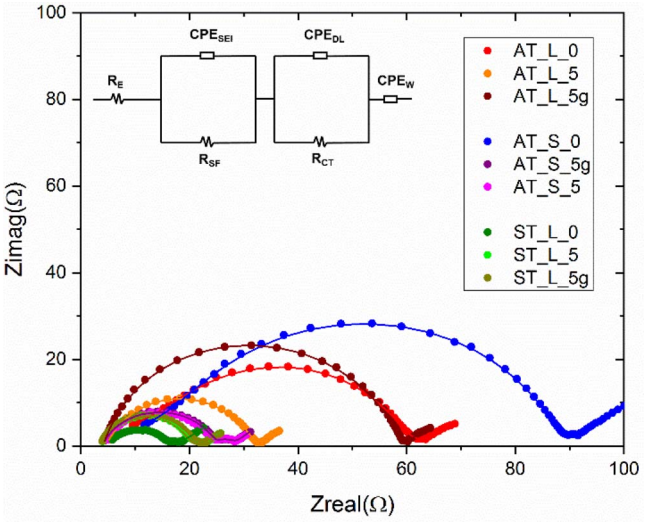


**Figure 11.** Nyquist plot of measured impedance spectrum and fit curve of $LiNi_{0.5}Mn_{1.5}O_4$ samples at SOC of 90% for one selected cell per sample.

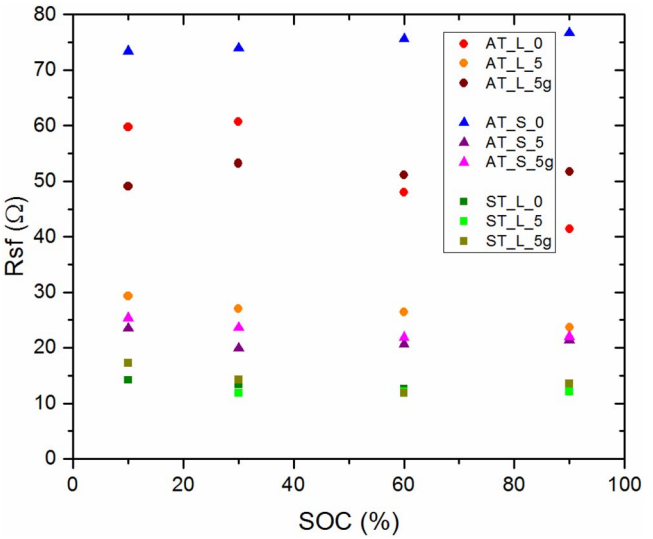


**Figure 13.** Result from equivalent circuit analysis fitted results of Rsf vs. SOC.

charge transfer resistance can be obtained by modeling with equivalent circuit analysis (Figure 12).

Figure 13 to Figure 15 show the results of the equivalent circuit analysis. The electrolyte resistance, surface film resistance, and the charge transfer resistances are the parameters which can be used to correlate material properties to kinetic properties. Figure 15 shows the electrolyte resistance (Re) at different SOCs. The electrolyte resistance (Re) can be described as a part of all ohm's resistances. Because the other ohm's residences are significantly smaller than the electrolyte resistance (Re) they can be neglected. According to the electrolyte resistance (Re) the conductivity (σ) can be estimated using the thickness of the electrolyte film (0.052 cm) and the electrode contact area to the electrolyte (0.013 $cm^2$). In general, the electrolyte resistance of all materials is between 3 Ω and 7 Ω. Apart from material morphology, the deviation in the values might be due to the handling of these coin cells while assembling and general errors which can occur. Figure 13 shows the surface film resistance at different SOCs. The surface film resistance of the material can be correlated the stability of the cathode material surface against the reactive electrolyte. According to the surface film thickness, the surface film resistance values differ. From this interpretation, it is possible to estimate the magnitude of electrolyte decomposition of different materials. Figure 13 reveals that the surface film resistance at different SOCs only changes slightly. A speculated passivating film formation cannot be seen during the change of the SOC. Figure 13 shows that the untreated "spray drying" material (ST_L_0) has a very low surface film resistance with 14 Ω at a SOC of 10%, whereas the untreated "pulse gas" samples (AT_S_0, AT_L_0) have a surface film resistance of 73 Ω and 59 Ω respectively. By additional calcination the surface film resistance values were significantly reduced to 23 Ω for the "pulse gas" suspension sample (AT_S_5), to 29 Ω for the "pulse gas" solution sample (AT_L_5) and to 17 Ω for the "spray drying" sample (ST_L_5). Additional grinding has further reduced the surface resistance as shown in Figure 13. The same interpretation can be applied for other SOCs. The correlation to the specific surface is clearly shown in Figure 16 where it can be seen that the reduction of the surface leads to a reduction in the surface film resistance. From the results of the different electrochemical methods (Table II) it can be concluded that the magnitude of parasitic reaction occurring in the cell is directly proportional to the specific surface area.

Figure 14 represents the charge transfer resistance at different SOCs. The charge transfer at an electrode/electrolyte interface is an essential process of the charge/discharge reaction of lithium-ion batteries. This phenomenon determines the reaction occurring in the electrode. In general, the charge transfer values for the different materials are heavily influenced by the SOC. From Figure 14 it can be seen that at a SOC of 90% the untreated "spray drying" material (ST_L_0) has a very low charge transfer resistance of 3 Ω, whereas the untreated "pulse gas" samples (AT_S_0, AT_L_0) show a charge transfer resistance of 17 Ω. By additional calcination, the charge transfer resis-

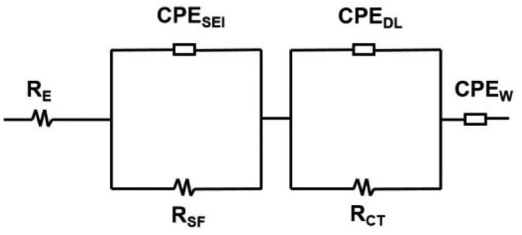


**Figure 12.** Equivalent circuit used for the EIS fit. ($R_E$: electrolyte resistance, $CPE_{SEI}$: Solid Electrolyte Interface Constant Phase Element, $R_{SF}$: Surface Film Resistance, $CPE_{DL}$: Double-Layer Constant Phase Element, $R_{CT}$: Charge Transfer Resistance, $CPE_W$: Warburg Resistance Constant Phase Element).

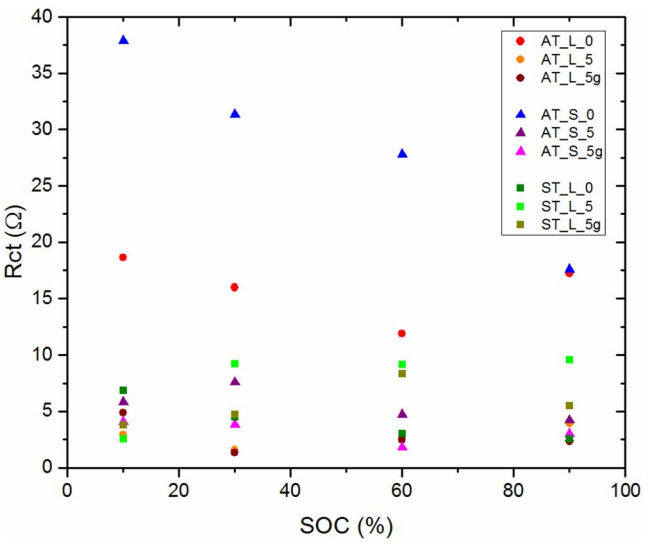


**Figure 14.** Result from equivalent circuit analysis fitted results of Rct vs. SOC.

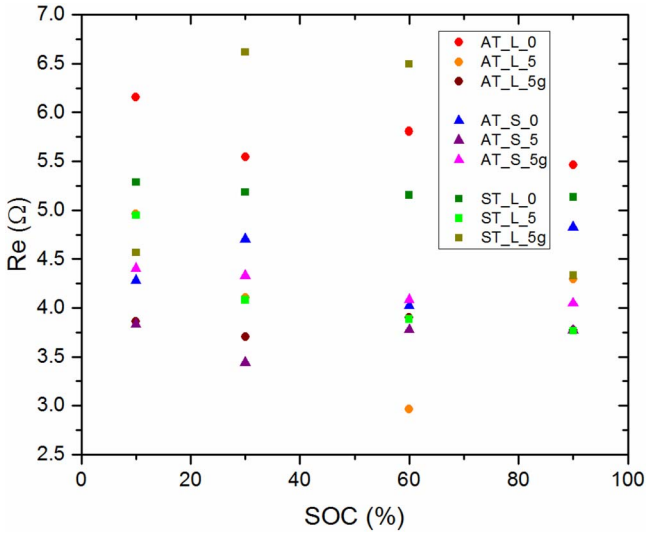


**Figure 15.** Result from equivalent circuit analysis fitted results of Re vs. SOC.

tance was significantly reduced to 4 Ω for the "pulse gas" samples (AT_S_5, AT_L_5) and increased to 9 Ω for the "spray drying" samples (ST_L_5). Additional grinding has further reduced the charge transfer resistance for all materials as shown in Figure 14. The same trend can be applicable for other SOCs which mentioned. The charge transfer resistance is directly influenced by the particle size and pore size distribution within the electrode layer. It is determined by the particle to particle contact as well as the continuous crystal network within the electrode layer. This continuous crystal network provides an improved electrode and electrolyte interface inside the porous electrode. As expected, the not well-crystallized materials (AT_L, AT_S and ST_L) possess higher charge transfer resistances than the other materials.

## Conclusions

The influence of the different synthesis routes on the electrochemical performance and the electrolyte decomposition was studied. It was shown that the $LiNi_{0.5}Mn_{1.5}O_4$ cathode material can be synthesized with a specific capacity of more than 130 mAh/g at 0.1 C by using and modifying different synthesis methods. From this work, it can be seen that additional calcination has a strong influence on the particle size and $Mn^{3+}$ reduction. The grinding process prior to additional calcination has only a small influence on the particle size level, but it has more impact on the aggregation and agglomeration of the materials, and thus on the particle size distribution. The material synthesized on the basis of a suspension exhibits a higher $Mn^{3+}$ amount than the solution based materials. To obtain optimum electrochemical performance, it is recommended to have a particle size of about 1 μm. Furthermore, it can be seen that the electrolyte decomposition is heavily influenced by the specific surface area of the material. To reduce capacity fading and kinetic hindrance, a uniform particle size distribution and appropriate particle sizes are necessary. It is also deduced that materials with a clear octahedron particle structure have improved electrochemical and kinetic properties and less electrolyte decomposition. This work shows that materials with bigger octahedron particles possess a low surface film resistance, as seen for the "spray dried" ground sample, whereas materials with a uniform particle size distribution possess a comparatively low charge transfer resistance, as seen for the "pulse gas" ground samples. This work suggests appropriate modifications that can help to improve the kinetic and the electrochemical properties of cathode materials. It also summarizes the different challenges which have to be overcome in order to upscale $LiNi_{0.5}Mn_{1.5}O_4$ while achieving the same electrochemical properties and reducing degradation.

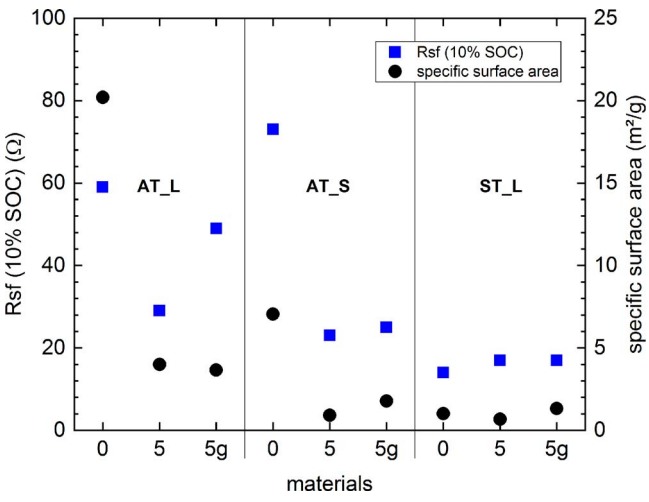


**Figure 16.** Correlation between specific surface area and surface film resistance of $LiNi_{0.5}Mn_{1.5}O_4$ samples.

## Acknowledgments

The authors acknowledge the support received as part of the project EMBATT2.0 (03XP0068G) funded by the German Federal Ministry of Education and Research (BMBF).

## ORCID

Matthias Seidel https://orcid.org/0000-0003-3993-783X

## References

1. X. Luo, J. Wang, M. Dooner, and J. Clarke, *Applied Energy*, **137**, 511 (2015).
2. M. Hu, X. Pang, and Z. Zhou, *J. Power Sources*, **237**, 229 (2013).
3. R. J. Gummow, A. de Kock, and M. M. Thackeray, *Solid State Ionics*, **69**(1), 59 (1994).
4. T. Minami, C. Iwakura, S. Kohjiya, I. Tanaka, M. Tatsumisago, and M. Wakihara, Editors, *Solid State Ionics for Batteries*, Tokyo, Springer (2005).
5. S. Malmgren Younesi, K. Edström, and S. Tan, *J. Solid State Electrochem (Journal of Solid State Electrochemistry)*, **18**(8), 2157 (2014).
6. J. Lee, N. Dupre, M. Avdeev, and B. Kang, *Scientific Reports*, **7**(1), 6728 (2017).
7. C. Zhu, C.-g. Han, and T. Akiyama, *RSC Adv*, **5**(62), 49831 (2015).
8. H. Duncan, B. Hai, M. Leskes, C. P. Grey, and G. Chen, *Chem. Mater.*, **26**(18), 5374 (2014).
9. Kenneth I. Ozoemena and Shaowei Chen, (Eds.), *Nanomaterials in advanced batteries and supercapacitors*, Cham, Springer (2016).
10. T. Eriksson, *$LiMn_2O_4$ as a Li-Ion battery cathode: From bulk to electrolyte interface, Uppsala, Acta Universitatis Upsaliensis*, (2001).
11. M. Börner, P. Niehoff, B. Vortmann, S. Nowak, M. Winter, and F. M. Schappacher, *Energy Technol.*, **4**(12), 1631 (2016).
12. P. Axmann, G. Gabrielli, and M. Wohlfahrt-Mehrens, *J. Power Sources*, **301**, 151 (2016).
13. J. Zheng, J. Xiao, X. Yu, L. Kovarik, M. Gu, F. Omenya, X. Chen, X.-Q. Yang, J. Liu, G. L. Graff, M. S. Whittingham, and J.-G. Zhang, *Phys. Chem. Chem. Phys.*, **14**(39), 13515 (2012).
14. S. Yang, *Int. J. Electrochem. Sci.*, 10847 (2016).
15. S. R. Li, C. H. Chen, and J. R. Dahn, *J. Electrochem. Soc.*, **160**(11), A2166 (2013).
16. S. R. Li, C. H. Chen, J. Camardese, and J. R. Dahn, *Journal of the Electrochemical Society*, **160**(9), A1517 (2013).
17. R. R. Richardson, M. A. Osborne, and D. A. Howey, *J. Power Sources*, **357**, 209 (2017).
18. G. Gabrielli, P. Axmann, and M. Wohlfahrt-Mehrens, *J. Electrochem. Soc.*, **163**(3), A470 (2016).
19. A. J. Smith, J. C. Burns, D. Xiong, and J. R. Dahn, *J. Electrochem. Soc.*, **158**(10), A1136 (2011).
20. J. C. Burns, A. Kassam, N. N. Sinha, L. E. Downie, L. Solnickova, B. M. Way, and J. R. Dahn, *J. Electrochem. Soc.*, **160**(9), A1451 (2013).
21. S. R. Li, C. H. Chen, X. Xia, and J. R. Dahn, *J. Electrochem. Soc.*, **160**(9), A1524 (2013).
22. J. P. Meyers, M. Doyle, R. M. Darling, and J. Newman, *J. Electrochem. Soc.*, **147**(8), 2930 (2000).

23. L. Wang, J. Zhao, X. He, J. Gao, J. Li, C. Wan, and C. Jiang, *Int. J. Electrochem. Sci.*, **7**, 345 (2012).
24. Dr. Ulla Reutner, *Particle synthesis in pulsed hot gas stream*, https://www.glatt.com/de/news/termineeinzelansicht/datum/2016/04/14/particle-synthesis-in-pulsed-hot-gas-stream/.
25. D. Li, A. Ito, K. Kobayakawa, H. Noguchi, and Y. Sato, *Electrochimica Acta*, **52**(5), 1919 (2007).
26. T.-F. Yi, J. Mei, and Y.-R. Zhu, *J. Power Sources*, **316**, 85 (2016).
27. K. Amine, H. Tukamoto, H. Yasuda, and Y. Fuiita, *J. Electrochem. Soc.*, **143**(5), 1607 (1996).
28. B. Hai, A. K. Shukla, H. Duncan, and G. Chen, *J. Mater. Chem. A*, **1**(3), 759 (2013).
29. Z. Chen, S. Qiu, Y. Cao, X. Ai, K. Xie, X. Hong, and H. Yang, *J. Mater. Chem.*, **22**(34), 17768 (2012).
30. Q.-C. Zhuang, X.-Y. Qiu, S.-D. Xu, Y.-H. Qiang, and S.-G. Sun, in *Lithium Ion Batteries - New Developments*, I. Belharouak, Editor, 189, InTech (2012).